AIAA-2015-0827

Unsteady Aerodynamic Loads Effected by Flow Control on a Moving Axisymmetric Bluff Body

Thomas J. Lambert*, Bojan Vukasinovic† and Ari Glezer‡
Woodruff School of Mechanical Engineering,
Georgia Institute of Technology, Atlanta, GA 30332-0405

The coupling between a moving axisymmetric bluff body and its wake is modified in wind tunnel experiments using controlled interactions between an azimuthal array of fluidic actuators and the cross flow over its aft end. Enhancement or suppression of the flow coupling has profound effects on the global unsteady aerodynamic loads on the moving body and the evolution of its near wake. The model moves in six degrees of freedom along a prescribed trajectory using eight servo-controlled support wires with inline force transducers that are operated in closed-loop with feedback from a motion analysis system. Actuation is effected by an integrated azimuthal array of four aft-facing synthetic jet actuators around the perimeter of the tail end such that each actuator effects a time-dependent segment of local flow attachment over the aft surface. The present investigation focuses attention on the reciprocal relation between the response of the near- and far-wake to the actuation and the associated changes in the induced aerodynamic loads when the body executes nearly time-harmonic pitch over a range of reduced oscillation frequencies (up to $k = 0.26$). The response of the wake to stabilizing and destabilizing actuation programs that effect reduction or enhancement of the aerodynamic loads are investigated using particle image velocimetry (PIV) and hot wire anemometry in the near and far wake, respectively. It is shown that this flow control approach induces aerodynamic loads that are comparable to the loads on the baseline configuration, and therefore may be suitable for in-flight stabilization.

Nomenclature

A_J	actuator orifice cross-sectional area
A_w	area of wake bounded by 95% freestream
C_D	coefficient of drag
C_μ	jet momentum coefficient
D	axisymmetric body diameter
D_w	support wire diameter
f	body pitching frequency
f_{act}	synthetic jet frequency
F_D	aerodynamic drag force
F_L	aerodynamic lift force
h_s	body backward-facing step height
k	model reduced frequency
L	body chord length
m	vortex shedding mode
M_p	aerodynamic pitching moment
psd	power spectral density
q	planar velocity magnitude
R	axisymmetric body radius
R_c	Coanda surface radius
Re_D	Reynolds number
St_D	Strouhal number
t	time
u	streamwise velocity component
U_j	maximum jet expulsion velocity
U_0	free stream velocity
v	cross-stream velocity component
w	vertical velocity component
x	streamwise coordinate
y	cross-stream coordinate
z	vertical coordinate
z_w	centroid of wake bounded by 95% freestream
α_x	roll coordinate
α_y	pitch coordinate
α_z	yaw coordinate
ρ	air density
τ	body pitching period
τ_{conv}	body convective time scale
ϕ	phase lag relative to model pitching

* Graduate Research Assistant, AIAA Member.
† Research Engineer, AIAA Member.
‡ Professor, Associate Fellow AIAA.

I. Technical Background

The present work focuses on control of the global unsteady aerodynamic loads on a moving axisymmetric bluff body by modification of the coupling between the flow over the body and its near wake. The coupling is altered using azimuthally-segmented hybrid actuation that effects a time-dependent partial flow attachment of the nominally axisymmetric separating shear layer over the aft end of the body and thereby imposes asymmetric distortion of the near wake that has a profound effect on its evolution and stability (e.g., Wu et al.[1]). As part of this control strategy, attachment is effected using fluidic actuation frequencies that are sufficiently high above the receptivity bandwidth of the natural unstable modes of the near wake (e.g., Erk[2], Smith et al.[3], Amitay et al.[4], Honohan et al.[5], Glezer et al.[6]).

The effectiveness of active separation control strategies and thereby of global aerodynamic performance can be significantly enhanced by hybrid, active and passive control that exploits the interaction of the actuation jets with adjacent solid surfaces, or the Coanda effect that has been investigated extensively since the 1940s (e.g., Newman[7]). This effect has also been the basis of circulation control over lifting surfaces in numerous aerodynamic systems (e.g., Englar[8]). Another passive feature that can be used is a sharp leading edge to induce separation off an axisymmetric body that was controlled by jet injection further downstream[9]. Hybrid flow control was also demonstrated by Nagib et al.[10] who combined a short backward facing step with a jet to control local separation. This approach was also utilized for controlling internal flows, for example, by Lo et al.[11] who controlled separation in adverse pressure gradients in a diffuser.

Since the Coanda effect is associated with the attachment of an inherently separated flow to a solid surface, this flow configuration presents a unique opportunity to create net aerodynamic forces on various bluff bodies through controlled activation. Freund and Mungal[12] reduced the aerodynamic drag of axisymmetric bodies by up to 30% using induced attachment at the aft corner of the body by steady, circumferentially-uniform blowing over Coanda surfaces. Rinehart et al.[13,14] demonstrated generation of a asymmetric force on an aerodynamic platform using the interaction of a single synthetic jet with an integrated axisymmetric azimuthal Coanda tail surface along a backward facing step. In a related investigation, McMichael et al.[15] exploited this flow control approach to the separated base flow of an axisymmetric 40 mm spin-stabilized projectile to effect aerodynamic steering forces and moments that were sufficient to control the trajectory of the projectile in flight. Corke et al.[16] reported alteration of the drag and side forces on an axisymmetric body using tangential plasma actuation placed upstream of a Coanda surface. Abramson et al.[17,18] extended the Coanda actuation methodology to effect prescribed (asymmetric) side forces by using four individually-controlled azimuthally distributed synthetic jets within the rearward-facing step of the tail and demonstrated that the induced forces can be used to effect steering during flight and trajectory stabilization. Finally, Lambert et al.[19] showed that unstable motion of a free-moving axisymmetric model can be significantly suppressed or enhanced with appropriate timing and modulation of the actuation, and this could lead to significant directional control authority for free flight aerodynamic bodies.

Control of the aerodynamic forces on axisymmetric platforms builds on numerous earlier investigations of the uncontrolled base flow and its natural instabilities. The basic motions of spinning projectiles, including natural nutation and precession linear and nonlinear instabilities, induced by Magnus, damping, and normal forces and moments are discussed in detail in the classical work of Nicolaides[20]. The instabilities of symmetric projectiles in the presence and absence of spin were discussed in detail by Murphy[21]. While spin-stabilized projectiles are gyroscopically stable to axisymmetric moment instability, they are susceptible to roll resonance[22], and spin-yaw lock in[23], which add complicated non-linear effects to the projectile dynamics that are in general hard to correct for. In recent years considerable attention has been devoted to the development active control approaches for both fin- and spin-stabilized projectiles, including aerodynamic forces induced by a piezoelectric-articulated nose section[24], synthetic jet actuation on a spinning projectile[25], and the swerve response of finned and spin-stabilized projectiles to generic control forces[26,27].

An inherent difficulty with wind tunnel investigations of nominally 'free' aerodynamic bodies is related to their mounting in the tunnel's test section. Ideally, the model support should cause little or no aerodynamic interference (such as magnetic-force support[28]), but most conventional support systems have relied on some form of side or rear sting mounts that can interfere with the flow around the body and especially in its wake. An alternative support, aimed at minimizing flow interference, was utilized by Abramson et al.[17,18] and later on by Lambert et al.[29], who supported their model using thin wires. In the present investigations, an axisymmetric bluff body integrated with individually-controlled miniature fluidic actuators is wire-mounted on a programmable 6-DOF (x/y/z-translation & pitch/yaw/roll) eight-wire traverse that is electromechanically driven by a dedicated feedback controller to remove the parasitic mass and inertia of the dynamic support system and of the model. The interactions between the actuation and the cross flow are investigated using high-speed PIV, a motion analysis system, time-resolved aerodynamic forces and moments, and hot-wire anemometry.

The present investigations build on the earlier work of Lambert et al.[30] who demonstrated that *the aerodynamic loads induced by an azimuthal array of hybrid synthetic jet actuators on an axisymmetric bluff body are comparable to the corresponding aerodynamic loads that are generated during pitch motion over a broad range of frequencies in the absence of actuation and therefore can be explored for stabilization and steering*. These findings are illustrated in Figure 1. Hybrid actuation on the stationary model induces a lift force of up to ~0.65N (Figure 1a). The lift force on the body pitching at an amplitude of 3º and $k = 0.013$ in the absence of actuation (Figure 1b) varies nearly linearly with angle of attack with a maximum magnitude of ~0.85N at $\alpha = 3^{o}$. When the frequency is increased to $k = 0.259$ the maximum magnitude of the lift force decreases somewhat to ~0.75N (with a phase delay), and is still comparable to the actuation-induced force. The present investigations focuses on the effects of the actuation on the evolution of the wake and aerodynamic loads of body that is moving in prescribed pitch.

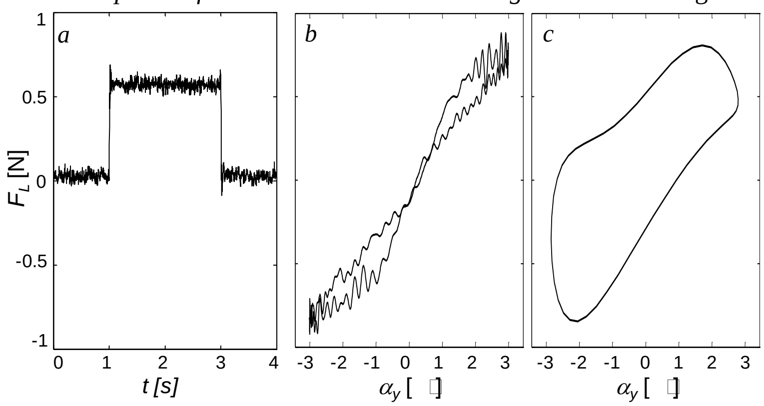

Figure 1. *Actuation induced lift force on a static model (a), and motion-induced lift force generated by pitching at a quasi-steady k = 0.013 (b), and unsteady k = 0.259 (c), by Lambert et. al.[30].*

II. Dynamic Wire Traverse and Experimental Setup

The axisymmetric model platform is wire mounted in an open-return wind tunnel at Georgia Tech (0.91 m x 0.91 m tests section, maximum speed of 40 m/sec) using an eight servo-motor traverse capable of motion in six degrees of freedom over a broad range of frequencies (Figure 2). The eight support steel wires ($D_w = 0.96$ mm) are selected to be thin enough to decouple their vortex shedding from the model, while thick enough to minimize translational and rotational vibrations. Each support wire is fastened to a servo motor, with an in-line load cell, and in addition, each motor is attached to an external spring for pretension. The flow control approach utilizes embedded synthetic jets in the axisymmetric model, where the connection for the actuators is enabled by means of electrical wires weaved along the back four support wires and through the tunnel walls, while the support wires provide electrical ground. The traverse is designed (based on earlier 1DOF investigations by Lambert et al[19]) to provide 3D translation up to 40 mm and angular motions in pitch, yaw and roll of up to 12º, 9º, and 6º, respectively at 1 Hz, with smaller amplitude motions up to 50 Hz. The forces and moments on the system (model and wires) are calculated from the measured load cell tensions projected onto the model, and the resulting aerodynamic forces and moments are computed relative to the wind-off conditions (the form drag load on each wire is also estimated). An external six-camera, high-speed motion analysis system tracks the model's motion in six degrees of freedom and is also used for feedback for the traverse controller.

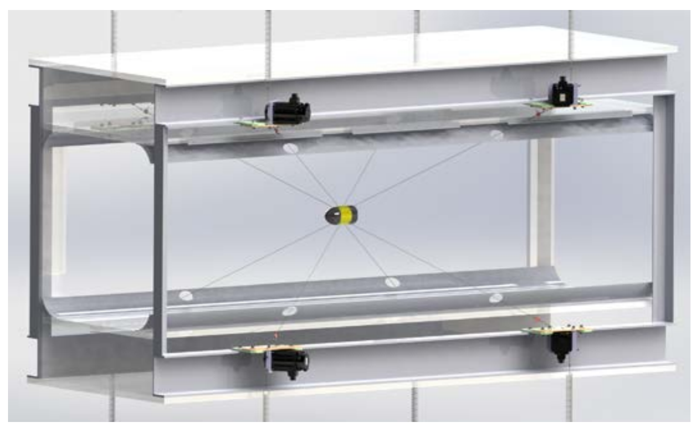

Figure 2. *Six-degree of freedom traversing mechanism utilizing eight support wires, each with an in-line load cell, a servo-actuator, and a pre-tensioned spring.*

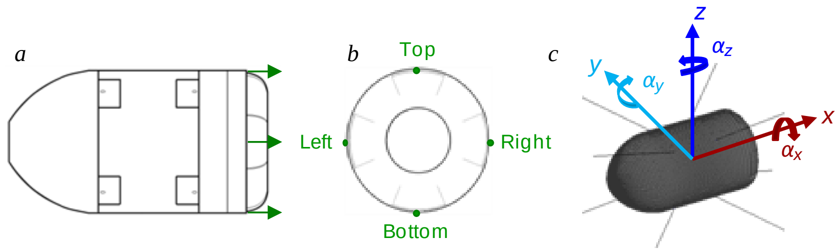

***Figure 3.** Side (a) and upstream (b) views of the centered wind tunnel model with four hybrid fluidic actuators marked in green, and the coordinate system for the 6-DOF traverse (c).*

The wind tunnel model ($D = 90$ mm, $L = 165$ mm, Re_D up to $2.4{\cdot}10^5$) is shown in Figures 3a and b (side and back, views). It is scaled based on the earlier investigations of McMichael et al.[15] and Abramson et al.[17,18]. The model is built using both stereo-lithographed and aluminum components. The eight support wires are fixed into the center aluminum piece, and the rest of the model containing the synthetic jet actuators is fastened together to the central aluminum spine. Aerodynamic control loads are generated using an azimuthal array of four aft facing independently-driven synthetic jet actuators (each measuring 0.38 × 34.3 mm) that are equally distributed around the perimeter of the tail section along a rear Coanda surface ($R_c = 12.7$ mm), which has grooves along the jet orifice edges that guide the jet flow with an adjoining backward-facing step 1.5mm high. Actuation leads to the partial attachment of the flow along the Coanda surface resulting in a reaction force by turning of the cross flow into the near wake. The model's motion in three translational (x, y, and z) and rotational degrees of freedom (roll, α_x, pitch, α_y, and yaw α_z) are depicted in Figure 3c. In the present investigations, the momentum coefficient of each jet is set to $C_\mu = 4{\cdot}10^{-3}$, at actuation frequency of $f_{act} = 1.1$kHz, the test section speed is varied up to $U_0 = 40$ m/s., and the model is moved in harmonic motion in pitch (α_y) with an amplitude of 3° at frequencies from 1Hz to 20Hz ($0.013 < k = \pi f L/U_0 < 0.259$).

Operation of the traverse utilizes a trajectory tracking controller shown in Figure 4. The two command inputs are a time trace for the model trajectory in six degrees of freedom, and an open-loop actuation time trace for the embedded synthetic jets. The commanded motion is converted into eight motor commands in an inner control loop involving only the motor encoders and load cells with a PID controller for disturbance rejection. In addition, an external motion analysis system is implemented to measure the real-time position of the model in 6DOF. This position measurement is used in an outer control loop to adjust the command of the inner control loop to allow for accurate trajectory tracking with disturbance rejection. The outer loop uses a PID controller that is set such that the commanded and actual trajectories converge within ten seconds of the motion onset. The real time load cell tensions are used to extract the aerodynamic forces and moments on the model by measuring the net force on the model and subtracting the inertia and gravitational effects predicted by the model's measured trajectory.

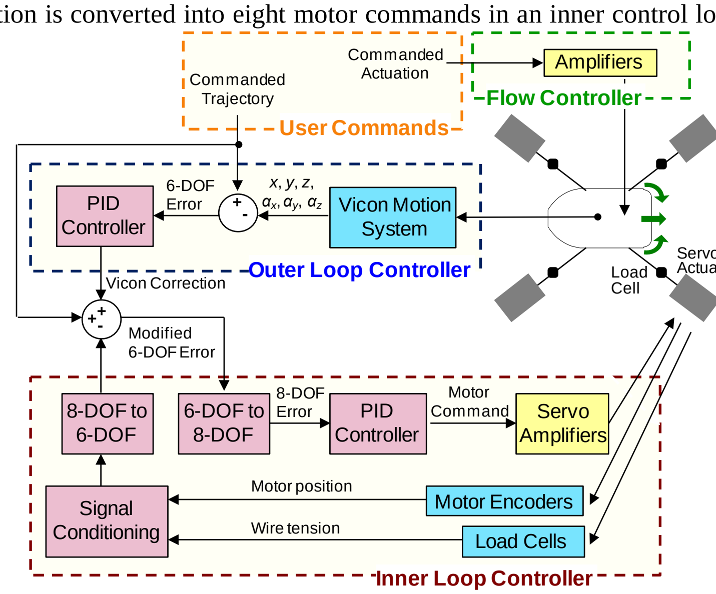

***Figure 4.** Schematics of the traverse trajectory tracking controller.*

III. The Far Wake of the Static Platform

The far wake of the base flow over the stationary platform aligned in the streamwise direction is documented at $x/D = 5$ using single-sensor hot wire measurements (sampled at 10 kHz) over a grid of 19 x 19 equally-spaced measurement points within the domain $-2 < z/R,\ y/R < 2$. Figure 5 shows color raster plots of the magnitude of the normalized velocity, q/U_0 at $U_0 = 40$m/s. The time-averaged velocity distribution in Figure 5a illustrates the radial extent of the far wake (note that the wake of the support wires is also sensed at this streamwise location which is approximately $900D_w$ downstream). Lambert et al.[26] showed that the measured aerodynamic drag is within 5% of the expected drag when the drag of the support wires is accounted for, indicating a negligible coupling. A continuous record of the time-resolved velocity magnitude $q(z;\ x = 5D,\ y = 0)$ across the wake's center plane

($y/R = 0$) is shown for reference in Figure 5b for $0 < t/\tau_{conv} < 400$ ($\tau_{conv} = D/U_0$), and demonstrates that the wake's width based on (say) $0.92U_o$ is approximately $0.9R$ (cf. Figure 7c).

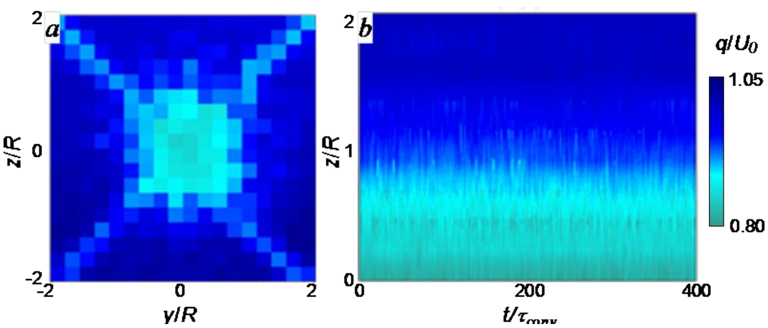

Figure 5. *Color raster plots of the velocity magnitude measured at $x/D = 5$ ($U_0 = 40$m/s) downstream of the model: a) time averaged in the y-z plane, and (b) time traces along $y = 0$.*

The corresponding power spectra of the velocity magnitude (Figure 5b) is shown in Figure 6 over a range of $2.25 \cdot 10^{-3} < St_D = fU_o/D < 2.25$. These spectra exhibit two notable spectral features. First, a spectral peak $St_D = 0.237$ is present at the edge of the wake ($z/R = 1$) and is attributed to shedding at the wake's dominant mode $m = \pm 1$ (the measurements of Rigas et al.[31] showed that this peak is just above $St_D = 0.2$). A second, low-frequency ($St_D = 2.25 \cdot 10^{-3}$) broad spectral peak is also detected near the edge of the wake ($z/R = 1$). As shown by Rigas et al.[31], this spectral peak is associated with slow ($St_D \approx 0.002$) axis switching of the dominant shedding mode $m = \pm 1$. This spectral map shows not only the dominant frequencies of the base flow, but also indicate spatial bounds (within the measurement plane) of their amplification, which are inherently linked to the flow stability features. The radial extent of the wake is also evident in these spectra as the power over the entire frequency range drops sharply beyond $z/R > 1.5$. In addition, the power at all frequencies also diminishes around the centerline of the wake ($z/R < 0.3$) indicating the absence (or diminution) of the mode $m = 0$.

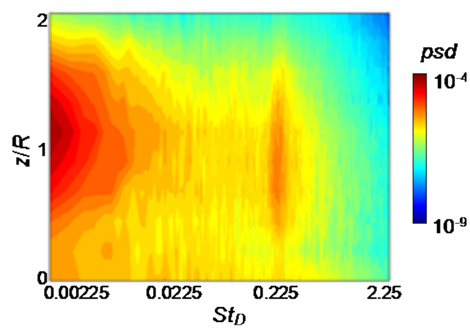

Figure 6. *Color raster plots of power spectra of the velocity magnitude along $y = 0$ ($x/D = 5$ and $U_o = 40$m/s).*

The variation of the frequency and magnitude of the peak spectral component $m = \pm 1$ over a range of Re_D ($1.44 \cdot 10^5 < Re_D < 2.31 \cdot 10^5$) are shown in in Figures 7a and b. These figures show the frequency and magnitude of these spectral peaks along two orthogonal axes ($z = 0$ and $y = 0$) through the centerline of the model. As in Figure 6, the spectral maps for $1.44 \cdot 10^5 < Re_D < 2.31 \cdot 10^5$ (not shown) also show that these peaks are nominally centered near the edge of the wake at ($y/R \approx 1$, $z = 0$) and ($y = 0$, $z/R \approx 1$) indicating that the time-averaged signature of $m = \pm 1$ is indeed axisymmetric. Furthermore, Figures 7a and b show that the dimensionless frequency of the dominant mode ($St_D \approx 0.23$) is nearly invariant with Re_D over this range, and although the magnitude of this spectral component diminishes with increasing Re_D, (ostensibly owing to the increase in the overall spectral content with Re_D and broadening of the dominant peaks), the symmetry of this spectral component is quite good. Figure 7c shows that within the resolution of the present measurements, the (normalized) cross stream velocity distribution, and, in particular, of the velocity deficit in the wake are quite similar over the range of Re_D. The maximum velocity deficit on the centerline is about 20% of the free stream velocity, while the edge of the wake (based on $q/U_o = 0.99$) is at $z/R = 1.5$.

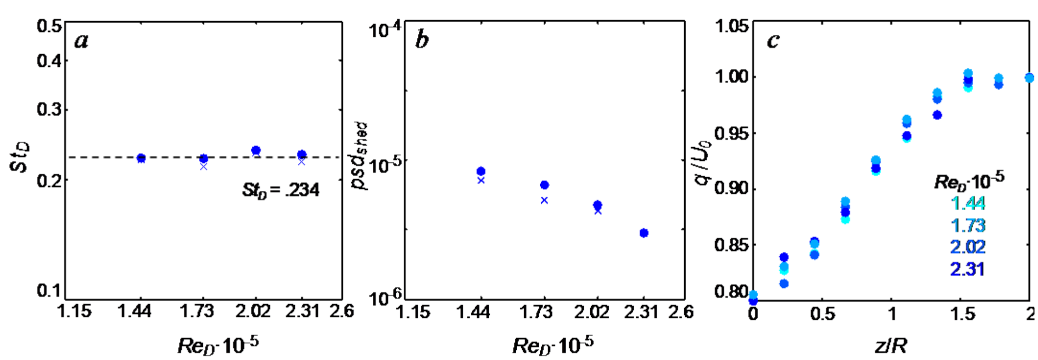

Figure 7. *Shedding peak Strouhal number (a) and power magnitude (b) with Re_D, as well as the time averaged planar velocity magnitude profiles (c) along the vertical (●) and horizontal (x) centerline at $x/D = 5$ with $Re_D = 1.44 – 2.31 \times 10^5$.*

The effects of actuation on the evolution of the far wake are investigated using the model's aft synthetic jet array ($Re_D = 2.31 \cdot 10^5$). Figure 8 shows corresponding time-averaged color raster plots of the velocity magnitude (overlaid with velocity vectors in the near wake) in the cross stream (x-z) plane of the near-wake (using PIV) and in the spanwise (y-z) plane of the far-wake (using hot wire anemometry). These data are presented in the absence of actuation (Figures 8a and b), and with continuous actuation using a single jet (at the top edge of the model centered at $y = 0$, $z/R = 1$, in Figures 8c and d) and a pair of opposing jets (at the top and bottom edges of the model centered at $y = 0$, $z/R = 1$ and $z/R = -1$, in Figures 8e and f). In the absence of actuation, (Figures 8a and d), the flow is reasonably symmetric about the body axis, where the near wake exhibits reversed flow within the domain $x/R < 2$. The corresponding distribution of the time-averaged velocity magnitude q/U_0 (Figure 8b) is duplicated from Figure 5a for reference and shows that overall the cross stream width of the wake based on $0.92U_0$ in the far field is narrower by about approximately 10%. When the top jet is activated ($C_\mu = 4 \cdot 10^{-3}$, Figure 8c) the upstream shear layer becomes partially attached to the Coanda surface and consequently, the flow along the top edge of the wake (based on $0.92U_0$) is deflected downwards at a nominal angle of 7.5°. It is noteworthy that the bottom edge of the near wake experiences less deflection and that the wake is primarily displaced downward without a significant change in its cross stream width as is evident at the downstream edge of the field of view (it also appears that the recirculating flow domain is shortened to $x/R < 1.8$). Figure 8d shows the respective deflection of the far wake. As expected, these data indicate that the deflection of the near field relaxes, and that the center of the wake is displaced vertically at a fixed distance ($\Delta z/R \sim 0.7$) relative to the centerline of the model, but that the cross section of the wake becomes distorted. When the top and bottom jets are activated simultaneously (Figures 8e and f, $C_\mu = 4 \cdot 10^{-3}$) the near wake is nominally symmetric relative to the centerline, the reversed flow domain is diminished (to $x/R < 1.5$) and the cross stream width of the wake becomes narrower (by about 10% relative to the base flow based on $0.92U_0$ at $x/R = 2.75$). The flow field in the y-z plane of the far field (Figure 8f) shows that the actuation leads to significant narrowing of the wake in the vertical (z) (by 30% relative to the far wake in the absence of actuation) and widening it in the horizontal (y) direction (by 40%) or increases its aspect ratio ($\Delta y/\Delta z$) to 1.33. As noted in the earlier investigation of Lambert et al.[30] , actuation by the top jet leads to a lift increment of 0.6N with virtually no change in drag, while the symmetric actuation by both the top and bottom jets results in a net increase of 0.1N in drag.

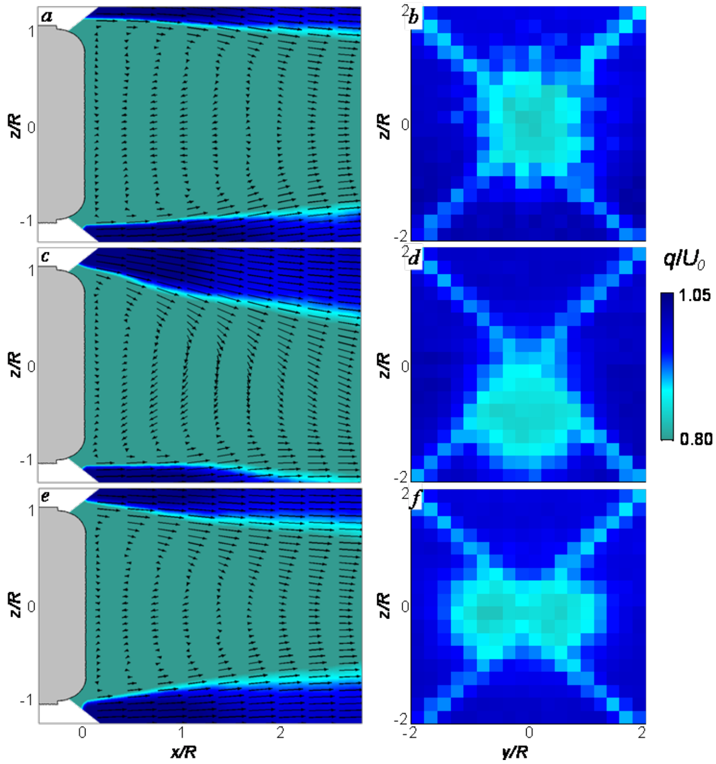

Figure 8. *Color raster plots of velocity magnitude in the near (a, c, and e) and far (x/D = 5, b, d, and f) wake of a stationary model (α_y = 0) in the absence (a,b), and presence of actuation (each actuator at $C_\mu = 4 \cdot 10^{-3}$): top actuator (c,d), top and bottom actuators (e,f). The near wake velocity distribution is overlaid with velocity vectors.*

The continuous actuation waveforms in Figures 8c-f are time-modulated to induce time dependent changes that couple to the evolution of the wake (and, consequently, in the induced aerodynamic loads on the model). This is implemented by activating the top and bottom jet pair so that they are operated out of phase during each half cycle of the time-harmonic modulating waveform (having modulation period τ_{mod}). The response of the wake clearly depends on the modulation frequency in a similar way to the dependence of the wake on pitch oscillations. Therefore, τ_{mod} for the *static* model is selected to be representative of quasi-steady, unsteady, and the (natural) vortex shedding (cf, Figure 6) pitch frequencies (k = 0.013, 0.259, and 1.425, respectively). The velocity magnitude in the far wake is measured phase-locked to the modulation waveform, and the maximum deflection of the far wake owing to the top jet is shown in Figure 9 for each modulation frequency (the base flow in the absence of actuation is shown in Figure 9a for reference). When the modulation frequency is quasi-steady (k = 0.013, Figure 9b), the wake is deflected downwards, and has a similar structure to the wake that is actuated by the top jet only (cf. Figure 8d). When the modulation rate is increased to $k = 0.259$ (Figure 9c), it appears that the unsteady actuation begins to couple to the "natural" shedding frequencies of the model and the wake shows some evidence of such coupling that results in spanwise asymmetry of the far wake. In Figure 9d the modulation frequency is approximately the vortex shedding frequency (cf. Figure 6), which distorts the wake (the mode $m = \pm 1$ appears to be locked to the preferred direction of oscillations) and significantly increases the vertical deflection and the domain and magnitude of the velocity deficit.

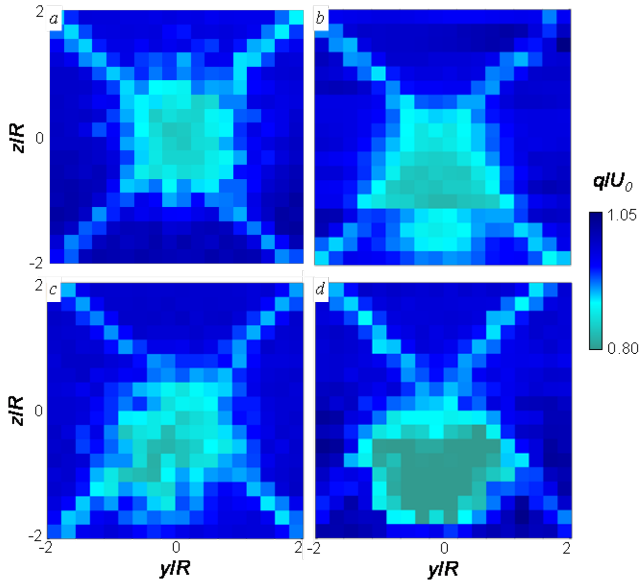

Figure 9. *Color raster plots of the peak deflection of the time averaged planar velocity magnitude, q, in the wake of the static model at x/D = 5 and U_0 = 40m/s for unactuated (a), and sinusoidal jet modulation with a max $C_\mu = 4\cdot 10^{-3}$ at an effective k = 0.013 (b), 0.259 (c), 1.425 (d).*

The centroid of the far wake is computed considering the wake boundary at $0.95U_0$ (and excluding the wakes of the support wires), using Fourier series to describe the azimuthal variation of the local radius. Phase-averaged (relative to the modulation signal), time traces of the wake centroid and area are shown in Figure 10. The top and bottom jets are active during $0 < t/\tau_{\mathrm{mod}} < 0.5$ and $0.5 < t/\tau_{\mathrm{mod}} < 1$, respectively. Traces are shown for modulation at k = 0.013, 0.259, and 1.425 (red, green, and blue, respectively, and the variations in the absence of actuation is shown in black for reference). As shown in Figure 10a, the wake of the base flow is nominally centered on the axis of the model. When k = 0.013, the wake is deflected at an amplitude of $z_w/R \sim 0.6$ and the deflection is in phase with the modulation waveform (i.e., the wake deflects downward when the top jet is active and vice versa). When k = 0.259 the wake is deflected at a lower amplitude $z_w/R \sim 0.3$, and its primary response lags the modulation by $\Delta\phi \sim 80^{\circ}$ which is attributed to the convective time scale. It is also noteworthy that the modulation response excites its fourth harmonic which is attributed to the coupling of the wake motion with a shedding frequency corresponding to St_D = 0.225, and it is argued that this coupling results in the spanwise asymmetry in Figure 9c. Modulation at k = 1.425 (equivalent to $St_D = 0.238$) leads to a 50% increase of amplitude of the quasi-steady deflection of the wake to $z_w/R \sim 0.9$. In addition, the phase lag of this wake is also $\Delta\phi \sim 80^{\circ}$, which is expected from the ratio of the reduced frequencies. The variation of the cross section area of the wake is Figure 10b shows the area of the $0.95U_0$ wake, which is nominally $1.35\pi R^2$ for the baseline, and fluctuates between 1.2-1.35 πR^2 for $k = 0.013$, $1.15\text{-}1.35\pi R^2$ for $k = 0.259$, and 1.1-1.35 πR^2 for $k = 1.425$. It is also interesting to note that the maximum wake area occurs at the central position of the wake for $k = 0.013$ and 0.259, but occurs at the maximum deflection of the wake for $k = 1.425$, which is attributed to the vortex shedding frequency interaction with the wake.

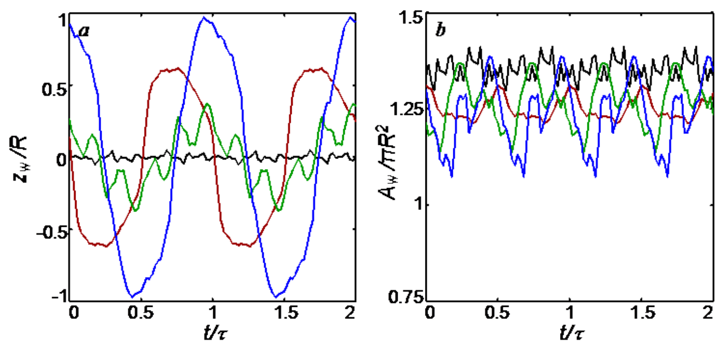

Figure 10. *Time traces of the wake centroid z_w (a) and its area A_w (b) bounded by $0.95U_0$ at x/D = 5 in the absence of actuation (black), and time harmonic modulation of the top and bottom actuator jets (max $C_\mu = 4\cdot 10^{-3}$) at k = 0.013 (red), 0.259 (green), and 1.425 (blue).*

IV. Controlled Flow over the Pitching Body

The effects of the actuation on the aerodynamic loads (drag, F_D, lift, F_L, and pitching moment, M_P) when the platform is moving in time-periodic (nearly harmonic) pitch at an amplitude of 3° are shown in Figures 11a,d and b,e and c,f, respectively for continuous actuation by the top jet and by both the top and bottom jets (the loads in the

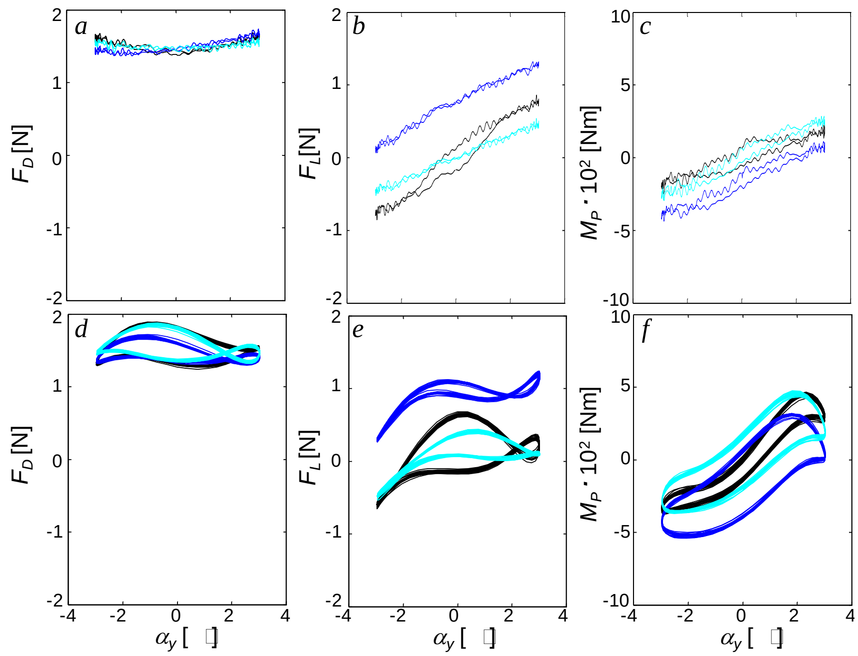

Figure 11. *Aerodynamic drag (a,d), lift (b,e), and pitching moment (c,f) during simple time-harmonic pitch at an amplitude of α_y = 3º and k = 0.013 (a-c), and 0.259 (d-f) during $450\tau_{conv}$ in the absence of actuation (black) and with actuation ($C_\mu = 4 \cdot 10^{-3}$) by the top jet (dark blue) and both jets (light blue).*

absence of actuation are also shown for reference). The variation of the loads with the pitch angle, α_y, are computed relative to the corresponding loads in the absence of flow in the test section to exclude inertial forces and the model's weight. The quasi-steady response (k = 0.013) is characterized in Figures 11a-c. Figure 11a shows that in the absence of actuation F_D = 1.5 N when $\alpha_y = 0$, corresponding to $C_D = F_D/(\pi R^2 \rho U_0^2) = 0.24$. Activation of the top jet leads to a similar response where the minimum of F_D is shifted to α_y = -2º. Activation of both jets leads to an increase of 0.1N in F_D at α_y = 0º, along with a 0.1 N decrease in F_D at the maximum extents of α_y. The variation of the lift force of the base flow with α_y (Figure 11b) exhibits a slight hysteresis and is nearly symmetric about $\alpha_y = 0$. When the top jet is activated the hysteresis vanishes and the nearly linear variation of the lift is offset by 0.6 N (relative to $\alpha_y = 0$), while when both jets are actuated the lift curve is offset back so that it is symmetric about $\alpha_y = 0$, but the magnitude of the lift at the ends of the pitch cycle is lower than the corresponding lift of the baseline indicating that the combined interaction of *both* jets with the oncoming flow leads to a small reduction in lift. The actuation of a single jet and then of the two jets (Figure 11c) leads to changes in pitch slopes from 0.006 to 0.007 to 0.008 Nm/deg, respectively where the top jet is centered around M_P = -0.02 Nm. The unsteady effects (k = 0.259), (Figures 11d-f), are characterized by significantly larger variations of the aerodynamic loads during the pitch cycle, with increased hysteresis due to increased coupling to the wake when the model's characteristic response time is commensurate with the wake's response time, as already discussed by Lambert et al.[30] Figure 11d shows that single jet actuation decreases the drag relative to the base flow during the upstroke while it is nearly identical to the drag of the base flow during the downstroke. When both jets are actuated the drag differences are primarily pronounced at the ends of the motion. It is interesting to note that the lift in the absence of actuation (the base flow, Figure 11e) is not completely antisymmetric about $\alpha_y = 0$, indicating that the motion of the model may not be symmetric (or purely time harmonic). Nevertheless, the lift in the presence of single jet actuation is offset relative to the base flow and exhibits significantly lower hysteresis. While the offset is removed in the presence of actuation by the two jets, the hysteresis is still lower compared to the base flow. As shown in Figure 10f, the pitching moment of the base flow is more antisymmetric and the effects of the actuation lead to an induced nose-down pitching moment and increased hysteresis while both actuators reduce the hysteresis somewhat from the top jet actuated case.

The earlier work of Lambert et al.[30] showed that appropriate modulation of the actuation waveform on the moving model can be used to manipulate the global aerodynamic loads. In the present work, the same actuation approach is utilized to demonstrate and investigate two limits of the actuation during the pitch cycle namely, direct reduction or augmentation of the lift force during the pitch cycle. In this approach the top and bottom actuators are operated out of phase during half the modulation cycle that coincides with the pitch cycle of the model (cf. Figure 10). To achieve quasi-steady reduction or augmentation of the lift (when the convective time scale is much shorter than the pitching period) the modulation is 180^0 out of phase and in phase and with the model motion, respectively. For unsteady reduction and augmentation (when the delay of the wake is taken in account), the modulation is effected at 220^0 and 40^0 out of phase with the model motion.

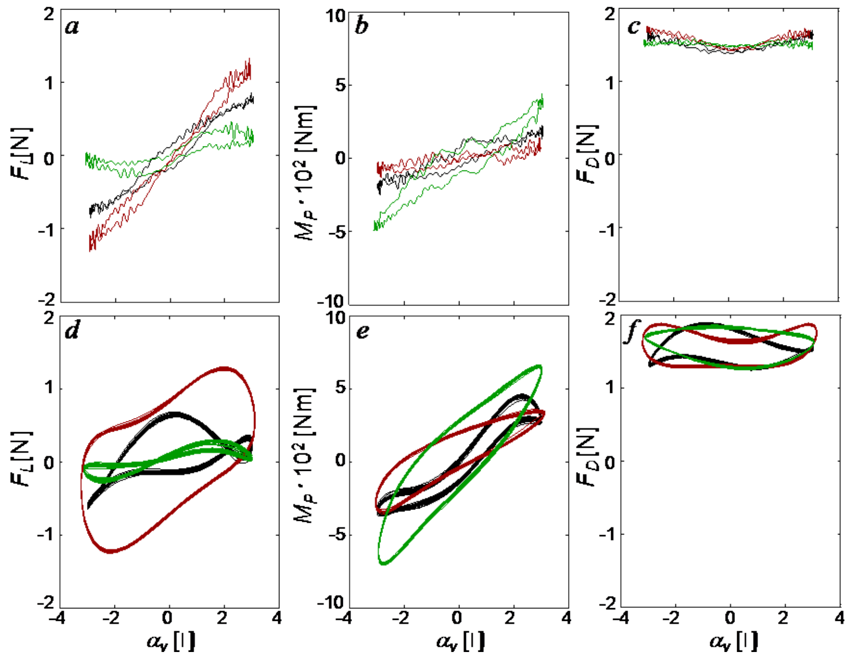

Figure 12. *Aerodynamic lift (a,d), pitching moment (b,e), and drag (c,f), during time-harmonic pitch at an amplitude of α_y = 3° and k = 0.013 (a-c), and 0.259 (d-f) during 450τ_{conv} in the absence of actuation (black) and actuation (C_μ = 4·10^{-3}) for lift reduction (green) and augmentation (red).*

Figure 12 shows the application of these actuation limits during the quasi-steady $k = 0.013$ (Figures 12a-c), and unsteady $k = 0.259$ (Figures 12d-f) pitch, and their effects on F_L (Figures 12a,d), M_P (Figures12b,e), and F_D (Figure 12c,f). Actuation during the quasi steady cycle (Figure 12a) shows that the lift can be significantly and symmetrically decreased or increased relative to the base flow (in the absence of actuation) such that the maximum lift is reduced from 0.9N to 0.4N or augmented to 1.3N leading to a 55% decrease or a 45% increase in the maximum force with small relative changes in hysteresis. The respective changes in the pitching moment (Figure 12b) show a 130% increase or 65% decrease in M_P with the corresponding reduction or augmentation of lift, which can be utilized for model steering and stabilization. The induced changes in the lift forces are quite significant at $k = 0.259$ (Figures 12d and e). The reduction in lift leads to a strong decrease in hysteresis compare to the base flow and, at the same time, an improved antisymmetry relative to $\alpha_y = 0$ with induced changes of 45% reduction and a 100% increase. The augmentation is accompanied by a significant increase in hysteresis. The corresponding changes in the pitching moment are 40% increase (with increased hysteresis) and 10% decrease. The effects of the actuation on the drag relative to the base flow at quasi-steady and unsteady motion (Figures 12c and f) are minimal. It is noteworthy that when the motion is unsteady, the nominally antisymmetric drag variation becomes nominally symmetric about $\alpha_y = 0$. Sections V and VI consider the evolution of the near and far wake in these two actuation limits.

V. Near Wake Response

The evolution of the near wake in time is characterized using PIV measurements that are acquired phase-locked to the time-periodic modulation waveform and to the pitch cycle (cf. Figure 12). Figure 13 shows phase-averaged color raster plots of the velocity magnitude in the *x-z* plane $q(z, t; x = R)$ during two pitching cycles at $k = 0.013$ ($\tau = 1$s) and pitching amplitude of 3°. In the absence of actuation (Figure 13a), the response of the near wake is in phase with the motion of the model's aft end. As the model pitches up ($0 < t/\tau < 0.5$) and down ($0.5 < t/\tau < 1$), the wake is deflected below and above the centerline, respectively. The largest change in velocity magnitude occurs through the shear layer near the cross stream edge of the wake when q/U_0 sharply increases from nearly 0.3 to 1 within $\Delta z/R \sim 0.1$. When the actuation leads to a reduction in the lift force (cf. Figure 12a), the wake response (Figure 13b) shows that the deflection amplitude of the

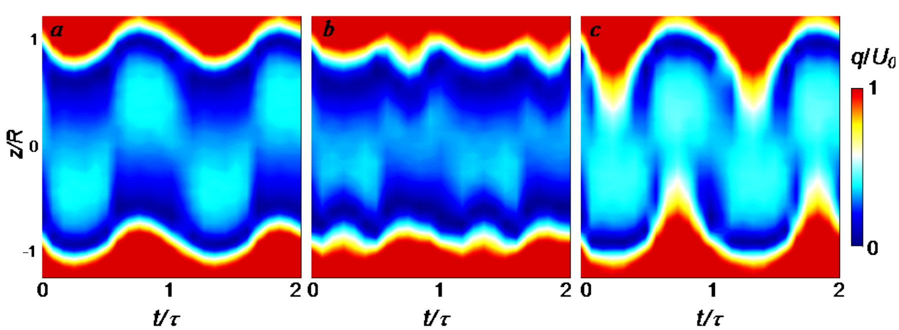

Figure 13. *Color raster plots of the phase-averaged velocity magnitude q(z, t; x = R) during harmonic motion at k = 0.013 in the absence of actuation (a) reduction (b) and augmentation (c) of lift.*

shear layer is reduced to 40% of its base flow level (Figures 13a), and the inner near wake becomes increasingly invariant with time even though the platform continues to pitch. *This shows that the actuation effectively decouples the response of the near wake from the pitching motion.* Figure 13c illustrates the realization of lift augmentation of Figure 12a, resulting in a significant increase (30%) in the deflection of the shear layer relative to the base flow (Figures 13a), and inducing a large difference in the distribution of the phase-locked variations in the velocity magnitude within the wake that are clearly synchronized with the pitch motion of the model. The actuation leads to an increase in the motion of the wake even though the motion of the model remains fixed.

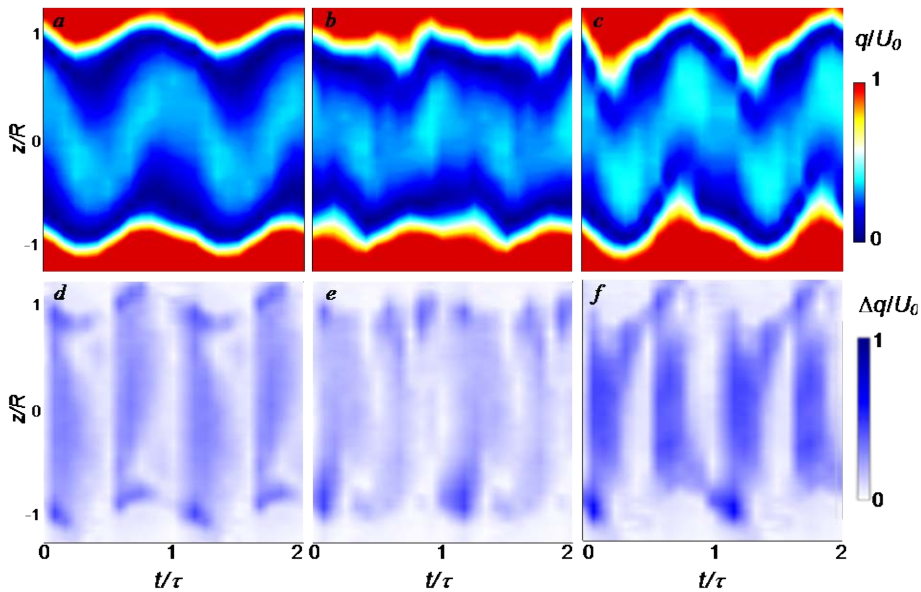

Figure 14. Color raster plots of the phase-averaged velocity magnitude q(z, t; x = R) during harmonic motion at k = 0.259 in the absence of actuation (a) reduction (b) and augmentation (c) of lift. The corresponding deviation of q(z, t; x = R) relative to k = 0.013 are shown in (d-f).

Similar to Figures 13a-c, the response of the wake at the higher frequency unsteady pitch ($k = 0.259$, $\tau = 0.05$s) is shown in Figures 14a-c. Although in general the response of the wake in Figures 14a-c is similar to Figures 13a-c, there are differences in both the magnitude and phase delays of the wake response, which are further emphasized by the difference in velocity magnitudes, Δq, of the unsteady and quasi-steady cases as shown in the raster plots in Figures 14d-f. First, Figure 14a shows that in the absence of actuation, the time periodic wake response is out of phase with the motion of the model's aft end. Although the model pitches up from t/τ = 0-0.5, the wake is deflected downward from t/τ = 0.1-0.6, showing approximately a $\Delta\phi = 45^o$ phase lag. While the change in the velocity across the edge of the wake is similar to Figure 13a, the time evolution of the inner flow appears to be more gradual than in the steady case, and the inner wake q also lags changes of q in the shear layer, which is another indication of the near wake unsteady response. The difference between the unsteady and quasi-steady responses are shown in Figure 14d, which shows two distinct regions, with a large velocity difference in the shear layer, and a smaller velocity difference in the wake core, as well as the diminishing difference towards the free stream. The flow that corresponds to lift reduction (Figure 14b) shows that the actuation leads to apparent decupling of the wake from the motion of the body with the shear layer deflections reduced to 50% of its base flow level. The difference between the near wake responses to the quasi-steady and unsteady lift force suppression actuation in Figure 14e shows that compared to the wake of the base flow there is no distinct different responses within the shear layer, but instead a much more uniform difference with the exception of two patches at z/R = -1 upon the onset of the bottom jet's actuation. The wake response to unsteady lift augmentation (Figure 14c) shows a 25% increase in the magnitude of deflection of the wake compared to the base flow. It is interesting to note that during augmentation of the unsteady lift, the inner core wake has less phase lag behind the outer shear layer than the unsteady base flow, showing that the actuation significantly altered the inner wake dynamics. During unsteady lift force augmentation the velocity within the inner wake is significantly lower than for quasi-steady lift augmentation (cf. Figure 13c). The augmentation difference between the unsteady and quasi-steady wake responses is shown in Figure 14f, where much stronger organization of the wake response is detected, as Δq has the same level of magnitude in both the wake core and the shear layer.

VI. Far Wake Response

To assess a 'far range' effect of the flow control schemes discussed in Section V, a detailed time-resolved characterization of the wake cross-section is done by the hot-wire anemometry, as already described in Section III.

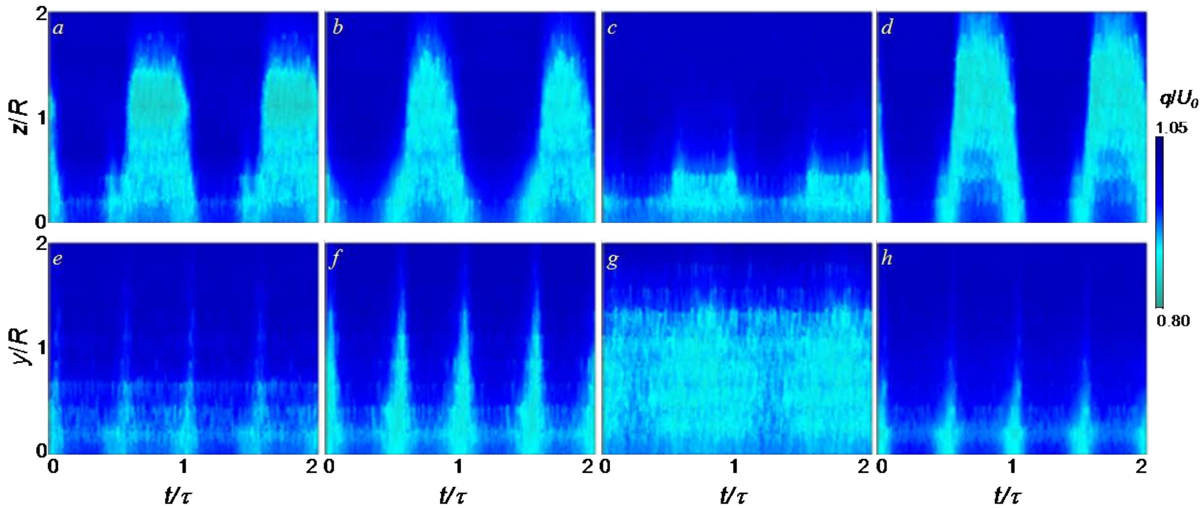

Figure 15. *Color raster plots of the time variation of the phase averaged velocity magnitude across the vertical (y/R = 0, 0 < z/R < 2) and horizontal (z/R = 0, 0 < y/R < 2) planes of the far wake when the model is stationary with active actuators (a,e), and when the model is pitching (k = 0.013) in the absence of actuation (b,f), and with actuation for lift reduction (c,g) and lift augmentation (d,h).*

Figure 15 shows raster plots of the normalized planar velocity magnitude, q/U_0 in the far wake at $x/R = 10$ at the free stream $U_0 = 40$m/s, analogous to the data presented in Figure 5b. Figures 15a-d show the vertical centerline of the far wake at $y/R = 0$, over a range of $z/R = 0$-2, and Figures 15e-f show the horizontal centerline at $z/R = 0$ over a range of $y/R = 0$-2. The results for the model pitching with quasi-steady reduced frequency $k = 0.013$ are shown in Figures 15b-d and 15f-h. For reference, the results for static and centered model are shown in Figures 15a and e. The force suppression and augmentation actuation schemes (Section V) are implemented in Figures 15c and g, and Figures 15a,d,e, and h, respectively. The unactuated cases are shown in Figures 15b and f. The unactuated far-wake response in the vertical direction to the quasi-steady model motion in Figure 15b shows an analogous response to the respective near wake case (compare Figures 13a and 15b). The wake motion is in phase with the motion of the model's aft end, with the major differences being the spread of the wake into the free stream (±1.15R in the near wake to ±1.8R in the far wake), and the evolved velocity profile in the far wake with only about 20% velocity deficit, as opposed to the recirculation and stagnation region of the near wake. The unactuated/natural wake response shows that the horizontal centerline extent of the wake is maximized when the wake passes through the center (compare Figures 15b and f), which leads to the predominant effect of the velocity magnitude in the horizontal direction to have double the frequency of the pitching motion. Figures 15a and e show the actuators being activated on the *static* model to induce the aerodynamic equivalent to the dynamic motion-induced force. These results show effectiveness of the timed actuation in mimicking the wake response to the body motion. However, it is also seen that the sinusoidal modulation of the actuation induces a faster far wake response than sinusoidal modulation of the motion, leading the wake response to appear more like a square wave (seen in Figure 15a), and consequently the wake residence time in the central position becomes diminished (see Figure 15e). The realization of the force suppression actuation is seen in Figures 15c and g which shows the effective far wake decoupling from the model motion, exhibiting small velocity variations in the vertical (Figure 15c), and virtually no variations in the horizontal (Figure 15g) direction. Another feature is that this resultant wake becomes compressed in the vertical and stretched in the horizontal direction, which results in an elliptical cross section. Contrary to the suppression scenario, the force augmentation actuation scheme induces increased amplitude of the wake oscillation in the vertical direction, by about 20% of the unactuated motion, which leads to the wake area extension in the vertical direction (Figures 15b and d), accompanied by a decrease in the wake extent in the horizontal direction (compare Figures 15f and h).

The frequency response of the planar velocity magnitude responses shown in Figure 15 are presented in Figure 16 in analogous fashion to the power spectra shown previously in Figure 6 for the static model. Each power spectrum in Figures 16a-h corresponds respectively to the flow conditions in Figure 15a-h. The unactuated response to the $k = 0.013$ sinusoidal pitching is shown in Figures 16b and f which still exhibit the two dominant frequency bands seen previously in the baseline spectra: the lower band which can be attributed to the axis switching of the dominant shedding mode, and the higher band associated with the vortex shedding. In addition, the superposed motion ($k = 0.013$) appears as bands at multiples of $St_D = 0.00225$ in the vertical direction (Figure 16b), and multiples of

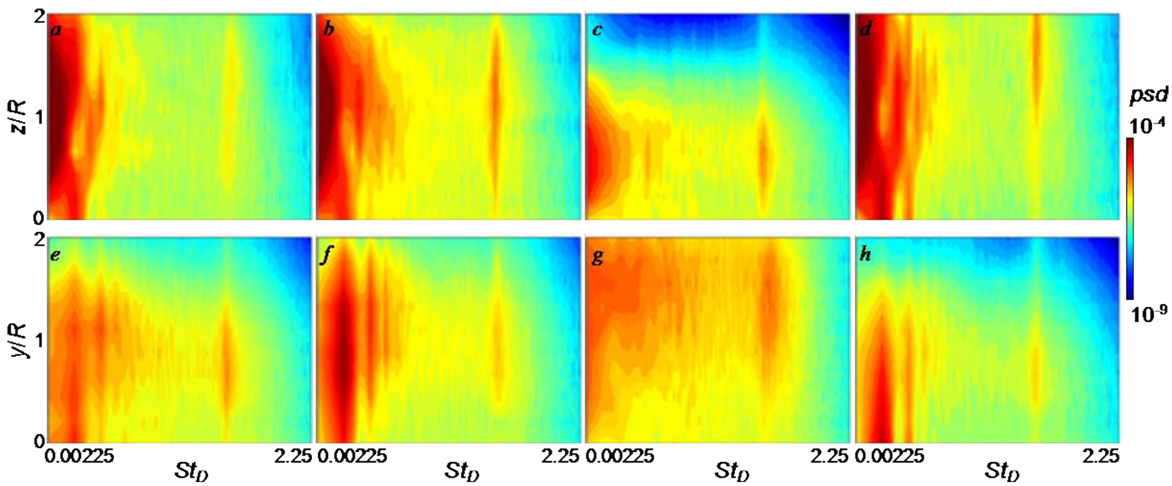

Figure 16. *Color raster plots of the power spectra corresponding to Figure 15.*

$St_D = 0.0045$ in the horizontal direction, and couples with the axis-switching mode. Figures 16a and e show a similar response when the model is held stationary and the force augmentation actuation is activated, with the exception that the actuation that mimics the model motion does not excite either the vortex shedding in the vertical direction or the axis switching in the horizontal direction as prominently as the actual model motion (Figures 16b and f). Upon the activation of suppression actuation, the power spectra becomes noticeably compressed in *z* (Figure 16c), and stretched in the *y* (Figure 16g) direction. This response has the frequencies attributed to the model motion and its harmonics effectively diminished, and the spectra becomes comparable to the baseline spectra compressed by ~75% in *z* and stretched by ~125% in *y* (compare Figures 16c and g with Figure 6). It should be also noted that the compression and expansion of the shedding frequency band is paired with the same alteration of the axis-switching frequencies. A different trend is seen upon force augmentation scenario, where the model motion and its harmonics are more prominent in their energy signatures, compared to the unactuated motion, but otherwise the augmented spectrum appears to be comparable to the unactuated frequency response stretched by ~125% in *z* and 75% in *y*.

The unsteady equivalent ($k = 0.259$) of the datasets analyzed in Figure 15a-h are presented in analogous fashion in Figures 17a-h, respectively. Comparing the unsteady unactuated flows in Figures 17b and f with the respective quasi-steady flow in Figures 15b and f, it is seen that the wake lags ~80° the body motion cycle, and the amplitude of vertical deflection is diminished by about 20%. This phase lag can be also estimated from ratio of distances multiplied by the near wake phase lag of $\phi = 45°$, which yields a visible lag of $\phi = 90°$, and is comparable to the $\phi \sim 80°$ observed in Figure 17b. In addition, the wake does not increase to free stream velocity at the centerline ($y/R = 0$) in the horizontal direction and this indicates that the wake development is such that it never fully extends past the centerline in the unsteady case, as it does in the steady case (compare Figure 17f and 15f). When the

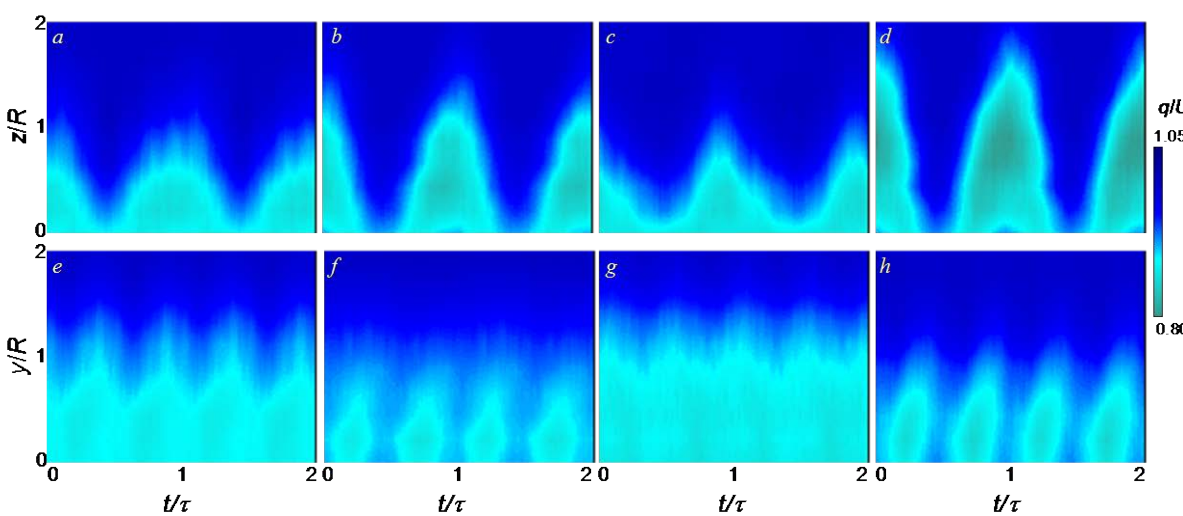

Figure 17. *Phase averaged velocity magnitude analogous to Figure 15 for k = 0.259.*

unsteady force augmentation actuation is applied on the static model to mimic the unactuated pitching wake, the far wake response does not match as it did in the quasi-steady case, reaching 75% of the baseline vertical amplitude, and stretching longer in the cross-stream direction. Consequently, the suppression case has more fluctuation then the quasi-steady equivalent (compare Figures 17c and g to 15c and g), although still significantly suppressing vertical fluctuations during the unactuated pitching by about 50%. Remarkably, the augmentation case is relatively more effective at the unsteady frequency, where the vertical deflection of the deficit region relative to the baseline is increased to 40% of the unactuated flow (compared to 20% in the quasi-steady flow), as seen in Figure 17d. The combination of the unsteady flow results in Figures 17b-d and f-h shows the same trend as in the quasi-steady results where force suppression acts to decouple the wake from the pitch motion, and stretches it in the cross-stream direction, while augmentation increases the wake coupling to pitching angle and compresses it in the cross-stream direction.

The unsteady frequency responses of the planar velocity magnitude shown in Figure 17 are presented in Figure 18 in analogous fashion to the power spectra shown previously in Figure 16. Each power spectrum in Figures 18a-h corresponds respectively to the same flow conditions in Figure 17a-h. One key feature that is noticeable in all of Figures 18a-h is significant reduction of the axis switching mode, even when the model is stationary and the actuation alone is applied at k = 0.259, as seen in Figures 18a and e. In this case without the model motion, the introduction of the k = 0.259 lift force augmentation actuation couples with the vortex shedding peak and excites the fourth harmonic (St_D ~ 0.225) as seen in Figure 18a, while not having this effect in the cross-stream (Figure 18e). The unactuated flow is presented in Figures 18b and f, and shows a broad spread of frequencies in the vortex shedding region (St_D ~ 0.234), and have noticeable peak bands corresponding to the model motion at St_D = 0.045 in the vertical and horizontal direction, each accompanied with a first harmonic. When implementing the suppression actuation scheme, the power spectra becomes noticeably compressed in z (shown in Figure 18c), and slightly stretched in y (shown in Figure 18g). Similar to the static model in Figure 18a, the actuation fourth harmonic near the shedding frequency is excited in the vertical direction, but is not excited in the cross-stream direction. Figures 18d and h show the unsteady augmentation actuation, with a significant, 40%, stretch in the vertical direction and 20% compression in the cross-stream direction (compare Figures 18d and h with 18 b and f). It is notable that the harmonics of the actuation in the augmentation case are significantly less noticeable than the harmonics in the jets alone or the suppression case (compare Figure 18d with Figures 18a and c), which may suggest that the coupling between the flow control actuation and the vortex shedding can be controlled on a dynamic model by the type of actuation chosen.

The resulting wakes presented in Figures 15 and 17 are quantified in Figure 19, using 50 points per cycle with 30 phase averages. The time traces of the vertical centroid (Figure 19a,c) and area (Figure 19b,d) of the wake bounded by 0.95U_0 and are presented in an analogous fashion to Figure 10. The quasi-steady wake at k = 0.013 is shown in Figures 19a,b and the unsteady wake at k = 0.013 is shown in Figures 19c,d. The unactuated response is shown in black, with the augmentation actuation in red and the cancellation actuation in green. In addition, the static model case from Figure 10 with the actuation by the top and bottom jets timed to mimic the pitching model is shown in blue, and the static unactuated model case is shown in dotted black. Figure 19a indicates a clear trend with the quasi-steady wake where the unactuated flow has a central deflection of z_w/R = ±0.6, and upon augmentation

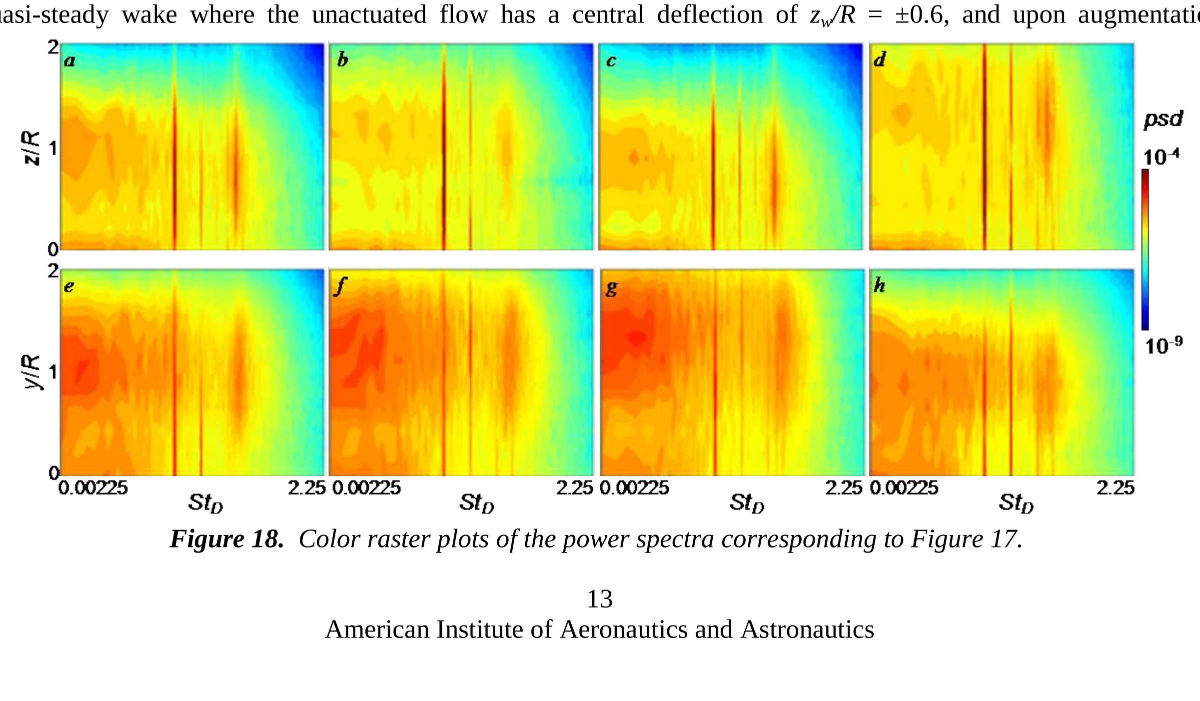

Figure 18. *Color raster plots of the power spectra corresponding to Figure 17.*

increases to deflections of $z_w/R = \pm0.8$, or upon suppression decreases to deflection of $z_w/R = \pm0.2$. In addition, the timed actuation on the static body nearly matches the unactuated pitching case with a deflection of $z_w/R = \pm0.5$, and having all wakes in phase with the model motion. Figure 19b shows that the unactuated wake area has a variation of 1.15-1.35πR^2 with maximum area at the centerline, and minimum area at the extremes. Upon force cancellation, the wake area becomes nearly invariant along the static baseline level, and upon amplification the wake area varies ~250% the unactuated level, while the flow control alone on a static model has 50% of the area variation of the baseline level. The unsteady wake shows some departure from the quasi-steady wake response, and also has a phase lag ~90° in the unactuated and the amplified cases, and ~80° in the unactuated and actuation on a static model cases observed in Figure 19c. The unactuated response of the wake at this frequency has a central deflection of $z_w/R = \pm0.5$, and upon augmentation increases to deflections of $z_w/R = \pm0.8$, and upon suppression decreases to deflection of $z_w/R = \pm0.25$, showing an increase in the efficacy of augmentation with a slight decrease in the efficacy of suppression. The stationary actuation case has a deflection of $z_w/R = \pm0.35$, or 70% of the unactuated level. It is interesting to note that the actuation alone case and the lift suppression include an excitation of the fourth harmonic, which is attributed to coupling with the vortex shedding frequency as described in the discussion of Figure 10, but the excitations of this frequency in the unactuated and lift augmentation wakes are less evident. This suggests that to achieve further decoupling of the wake from the model motion, the actuation may need to include a second modulation frequency that also suppresses the excitation of the harmonic closest to the vortex shedding frequency. The area variation of the 0.95U_0 bounded wake vs. time is a lot less structured at the unsteady frequency compared to the steady frequency (compare Figures 19b and d), with little variation of the area in the unactuated pitching case, and with a variation of 1.15-1.35πR^2 in the presence of all three actuation cases at $k = 0.259$.

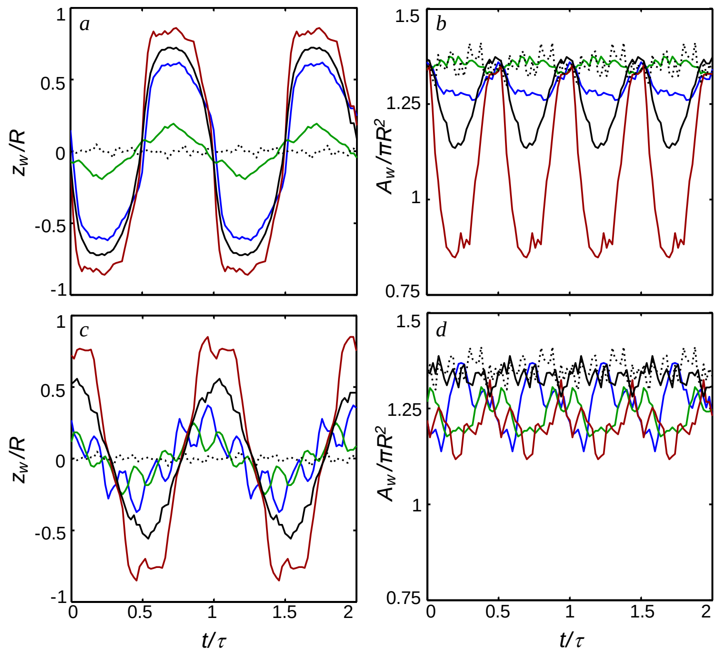

Figure 19. *Time traces of the wake centroid, z_w (a,c), and area, A_w (b,d) for k = 0.013 (a,b) and 0.259 (c,d) in the absence of actuation (black), and reduction (green) and augmentation (red) of the lift. The wakes of the static model in the presence (blue) and absence (dashed black) of actuation are shown for reference.*

VIII. Conclusions

The global unsteady aerodynamic loads on a moving axisymmetric bluff body are controlled by modification of the coupling between the flow over body and its near wake using an azimuthal array of four synthetic jet actuators around the perimeter of the body's aft end. The segmented hybrid actuation results in a time-dependent partial flow attachment of the nominally axisymmetric separating shear layer of the base flow over the aft end of the body, and the asymmetric changes have a profound effect on the evolution and stability of the near wake. The model translates along a prescribed trajectory using a 6 DOF traverse comprised of eight support wires that are independently servo-controlled in closed-loop with feedback from a motion analysis system. The present investigation focuses on the response of the near- and far-wake ($0 < x/D < 1.37$, and $x/D = 5$, respectively) to the actuation and the concomitant changes in the induced aerodynamic loads when the body executes simple, time-harmonic pitch over a range of reduced oscillation frequencies (up to $k = 0.26$). The flow evolution is characterized using high-resolution PIV measurements within a plane that is normal to the pitch axis and spans the entire near wake, while the far wake is characterized using hot-wire measurements in a plane that is normal to the streamwise direction, five diameters downstream from the model's aft end.

Active control is effected by time dependent modulation of the resonance waveform of a pair of opposite synthetic jets whose centerlines are within the pitch plane and the modulation is applied over a range of reduced frequencies $0.013 < k < 1.43$. The present investigations have demonstrated that the actuation can alter the evolution of the wake when the model is stationary in a manner that is similar to the effects of the model's pitch motion in the absence of actuation. The induced near-wake dynamic characteristics that are directly effected by the actuation are advected by the flow and are also detected farther downstream. While at a lower reduced frequency, the effects of the actuation on the global wake characteristics are nearly identical to the corresponding flow features of the uncontrolled flow over the pitching body, the control authority at a fixed actuation level diminishes somewhat as k increases to 0.259. However, at the highest modulation frequency $k = 1.43$ (which corresponds to the dominant natural wake frequency), the actuation directly amplifies the natural wake response. As expected, at reduced frequencies that correspond to the model's motion, such wake dynamics result in aerodynamic loads that that are similar to the loads on the uncontrolled pitching model.

Further attributes of the actuation are demonstrated on the model pitching at two disparate frequencies, namely quasi-steady (e.g., $k = 0.013$) when the wake response during a given phase of the oscillation is similar to that of the a static orientation at the same pitch angle, and unsteady (e.g., $k = 0.259$) when there is a significant phase lag between the wake response and the body motion. Spatial and spectral characterization of the far wake of the pitching model indicate three dominant spectral bands: ***i.*** the pitching frequency (and its higher harmonics), ***ii.*** a narrow-band high frequency corresponding to vortex shedding ($St \approx 0.234$), and ***iii.*** a broad low frequency band ($St \approx 2 \cdot 10^{-3}$) that is attributed to axis switching of the vortex shedding[36]. Two flow control strategies are applied to the dynamic model. The first strategy focuses on decoupling the wake response from the model pitching, therefore rendering the wake response equivalent to the wake of a nominally static model. The second strategy is designed to enhance the response of the wake to the prescribed motion of the body, as if the body is oscillating at a higher pitch amplitude. The results show that both the dynamics of the near- and far-wake are significantly decoupled from the model pitching when the pitching cycle aerodynamic lift force is deliberately diminished by the actuation, causing diminutions of 80% and 50% in the wake excursion at $k = 0.013$ and 0.259, respectively. Aerodynamic lift force during the active enhancement of the wake response increases the wake's excursion by 20% and 40% at $k = 0.013$ and 0.259, respectively. These changes in the wake dynamics concomitantly alter the global aerodynamic forces and moments, leading to about a 50% increase or decrease in the dynamic lift force or pitching moment, depending on the flow control strategy. A similar approach may be applied for stabilization or accelerated maneuvering of an equivalent airborne body.

Acknowledgment

This work has been supported by Georgia Tech and the Army Research Office.

References

[1]Wu, J.-Z., Lu, X.-Y., Denny, A. G., Fan, M., and Wu, J.-M., "Post Stall Flow Control on an Airfoil by Local Unsteady Forcing," *Journal of Fluid Mechanics*, Vol. 371, 21-58, 1998.

[2]Erk, P. P., "Separation Control on a Post-stall Airfoil using Acoustically Generated Perturbations", PhD Thesis, Tech. Univ. Berlin, Germany, 1997.

[3]Smith, D. R., Amitay, M., Kibens, V., Parekh, D., and Glezer, A., "Modification of Lifting Body Aerodynamics Using Synthetic Jet Actuators", *AIAA Paper* 1998-0209, 1998.

[4]Amitay, M., Smith, D. R., Kibens, V., Parekh, D. E., and Glezer, A., "Aerodynamic Flow Control over an Unconventional Airfoil Using Synthetic Jet Actuators", *AIAA J.*, Vol. 39, 2001, pp. 361-370.

[5]Honohan, A. M., Amitay, M., and Glezer, A., "Aerodynamic Control using Synthetic Jets", *AIAA Paper* 2000-2401, 2000.

[6]Glezer, A., Amitay, M., and Honohan, A. "Aspects of Low- and High-Frequency Actuation for Aerodynamic Flow Control," *AIAA Journal*, Vol. 43, 1501-1511, 2005.

[7]Newman, B.G., "The Deflexion of Plane Jets by Adjacent Boundaries-Coanda Effect", *Boundary Layer and Flow Control Principles and Applications*, Vol. 1, 1961, pp. 232-264.

[8]Englar, Robert J., "Circulation Control Pneumatic Aerodynamics: Blown Force and Moment Augmentation and Modification; Past, Present, & Future", AIAA Paper 2000-2541.

[9]Sigurdson. L. W., "The Structure and Control of a Turbulent Reattaching Flow", *J. Fluid Mech*., Vol. 298, 1995, pp. 139-165.

[10]Nagib, H. M., Reisenthel, P. H., and Koga, D. J. "On the Dynamical Scaling of Forced Unsteady Flows", *AIAA Paper* 1985-0553, 1985.

[11]Lo, K. P., Elkins, C. J., Eaton, J. K., "Separation Control in a Conical Diffuser with an Annular Inlet: Center Body Wake Separation", Exp. Fluids, Vol 53, 2012, pp 1317-1326.

[12]Freund, J. B., Mungal, M. G., "Drag and Wake Modification of Axisymmetric Bluff Bodies Using Coanda Blowing", *J. Aircraft*, Vol. 31, 1994, pp. 572-578

[13]Rinehart, C., McMichael, J. M., and Glezer, A., "Transitory Flow and Force Development on a Body of Revolution Using Synthetic Jet Actuation", *AIAA Paper* 2003-0618, 2003.

[14]Rinehart, C., "Aerodynamic Forces Induced by Controlled Transitory Flow on a Body of Revolution", Ph. D. Thesis, Georgia Institute of Technology, 2011.

[15]McMichael, J., Lovas, A., Plostins, P., Sahu J., Brown, G., and Glezer, A., “Microadaptive Flow Control Applied to a Spinning Projectile”, *AIAA Paper* 2004-2512, 2004.

[16]Corke, T. C., Tillotson, D., Patel, M. P., Su, W. J., Toldeo, W., "Radius Flow Vectoring for Projectile Drag and Steering Control Using Plasma Actuators", *AIAA Paper* 2008-3769, 2008.

[17]Abramson, P., Vukasinovic, B, and Glezer, A., “Direct Measurements of Controlled Aerodynamic Forces on a Wire-suspended Axisymmetric Body”, *Exp. Fluids*, Vol. 50, 2011, pp. 1711-1725.

[18]Abramson, P., Vukasinovic, B., and Glezer, A., Fluidic Control of Aerodynamic Forces on a Bluff Body of Revolution, *AIAA J.*, Vol. 50, pp.832-843, 2012.

[19]Lambert, T. J., Vukasinovic, B., and Glezer, A. "Yaw Control of a Moving Axisymmetric Body using Synthetic Jets", *AIAA Paper* 2013-0106, 2013.

[20]Nicolaides, J. D., "A History of Ordnance Flight Dynamics", AIAA Paper *70-533*, 1970.

[21]Murphy, C. H., "Symmetric Missile Dynamic Instabilities", *AIAA J. Guidance and Control*, Vol. 4, No. 5, *80-0320R*, 1980.

[22]Price Jr., D. A., "Sources, Mechanisms, and Control of Roll Resonance Phenomena for Sounding Rockets.", *AIAA J. Spacecraft*, **4**, No. 11, 1516-1521, 1967.

[23]Murphy, C. H., "Some Special Cases of Spin-Yaw Lock In", US Army Ballistic Research Laboratory, BRL-MR-3609, 1987.

[24]Barrett, R. M., Lee, G. M., “Design and Testing of Piezoelectric Flight Control Actuators for Hard Launch Munitions,” *Proc. SPIE* 5390, Smart Structures and Materials 2004: Smart Structures and Integrated Systems, 459, 2004.

[25]Sahu, J., "Time-Accurate Computations of Free-Flight Aerodynamics of a Spinning Projectile with and without Flow Control", AIAA Paper, 2006-6006.

[26]Ollerenshaw, D., Costello, M., “Model Predictive Control of a Direct Fire Projectile Equipped with Canards,” *Journal of Dynamic Systems, Measurement, and Control*, Vol. 130, 2008.

[27]Ollerenshaw, D., Costello, M., “Simplified Projectile Swerve Solution for General Control Inputs,” *Journal of Guidance, Control, and Dynamics*, Vol. 31, 1259-1265, 2008.

[28]Higuchi, H., Van Langen, P., Sawada, H., Timney, C. E., "Axial Flow Over a Blunt Circular Cylinder With and Without Shear Layer Reattachment", *J. Fluids Struct.*, Vol. 22, 1996, pp. 949-959.

[29]Lambert, T. J., Vukasinovic, B., and Glezer, A. "Unsteady Aerodynamic Flow Control of a Wire-Suspended, Moving Axisymmetric Body", *AIAA Paper* 2012-0073, 2012.

[30]Lambert, T. J., Vukasinovic, B., and Glezer, A. " Aerodynamic Flow Control of a Moving Axisymmetric Bluff Body", *AIAA Paper* 2014-0932, 2014.

[31]Rigas, G., Oxlade, A. R., Morgans, A. S., and Morrison. J. F. “Low-dimensional Dynamics of a Turbulent Axisymmetric Wake” *J. Fluid Mech.*, Vol. 755, R5, 2014.